The 2019 World Congress on
Advances in Structural Engineering and Mechanics (ASEM19)
Jeju Island, Korea, September 17 - 21, 2019

Equivalent hysteresis model for fiber elements of steel piers considering local instability effect

Hanqing Zhuge[1)] and Xu Xie[2)]

[1),2)]*College of Civil Engineering and Architecture, Zhejiang University, Zhejiang Province 310058, China.*
[1)] *11512058@zju.edu.cn*

ABSTRACT

In order to take account of local instability effect of steel plates in the fiber model, an equivalent hysteresis model for fiber elements of rectangular-section steel piers was proposed. Firstly, length of the effective damaged zone where local instability occurs was determined, and the average stress-average strain relationships of cross-section points over this area was extracted from calculation results of shell-element models which consider the elastoplastic large deformation. Then, based on the two-surface constitutive model of material, an equivalent hysteresis model was built up to fit the average stress–strain curve by introducing the equivalent elastic modulus, establishing the skeleton curve and reducing the radius of the bounding surface. Lastly, the fiber models where the elements in the damaged zone adopted the proposed equivalent hysteresis model were established. As a result , the seismic responses were quite similar with that obtained from the shell models under the same unidirectional or bidirectional seismic accelerations at the bottom of piers. Therefore, the equivalent hysteresis model proposed in this paper can provide a simplified and effective seismic response calculation method for seismic design of steel piers.

1.INTRODUCTION

Steel piers are seismically vulnerable components of steel bridges. In the 1995 Hanshin earthquake in Japan, many steel piers suffered severe damage [Kawashima et al. 1997], while local instability of steel plates was one of the most important failure modes [Usami 2017]. For this reason, in the past 20 years, many scholars have studied the local instability behavior of steel piers under earthquake actions and developed simplified calculation methods through experimentation and numerical simulation. Usami et al. regarded the state when load capacity decreased to 95% of its maximum as the limit state of the pier, and methods for evaluating the seismic performance of steel piers under unidirectional horizontal earthquakes were proposed [Ge et al. 1997, Ge et al. 2000, Usami et al. 2000, Usami et al. 2000].

[1)] PhD student
[2)] Professor

On the other hand, Watanabe et al. first found from an experimental study that under horizontal bidirectional quasi-static loads, steel piers have quite different seismic performance that under unidirectional loading [Watanabe et al. 2000]. Evaluation of seismic performance of piers maybe rather dangerous according to unidirectional loading. Since then, many scholars have studied the seismic performance of steel bridge piers under horizontal bi-direction earthquakes, and further confirmed the characteristics of seismic performance of structures are affected by the direction of earthquake actions. Based on the elastoplastic finite element analysis for steel piers, the seismic performance evaluation formulae were established for structures under the action of horizontal bidirectional earthquakes [Goto et al. 2006, Goto et al. 2007, Goto et al. 2009, Goto et al. 2009, Kulkarni et al. 2009, Kulkarni et al. 2012].

Compared with works on evaluating the structural seismic performance, there is still a lack of research on simplified methods for calculating the elastoplastic seismic response of steel piers during horizontal bidirectional earthquakes considering the local instability of steel plates. The FE method based on shell elements has a relatively high accuracy [Ge et al. 2000]; however, the modeling process is complex, calculation is large, and convergence is poor. At present, this method cannot be promoted and applied in engineering design. Therefore, using the advantages of considering fluctuant axial force and biaxial bending of fiber model, some scholars have established hysteresis models which can consider the local instability behavior of steel plates based on fiber elements. For example, an I-shaped beam was selected as the object, and the average stress–strain relationship of the effective damage area on the compression side of the section was used as the equivalent stress–strain relationship of fiber elements to consider the influence of the steel-plate local instability [Wang et al. 2012]. The model effectiveness was verified through quasi-static analysis; however, it has not been further verified under dynamic loading. The spacing between two diaphragms was regarded as the length of plastic hinge, and the box section was divided into three areas [Norika et al. 2003]. The average stress–strain relationships of these three regions within the length of the plastic hinge obtained from numerical analysis results of the shell model were selected as hysteresis relationships of fiber elements to consider the influence of local instability of steel plates. However, calculation accuracy cannot be guaranteed as the established average stress–strain relationship does not consider the influence of steel piers' structural parameters. Furthermore, this model cannot be applied to calculate horizontal bidirectional seismic responses. In addition, Dang et al. set a group of equivalent vertical nonlinear springs along the section of piers, and the influence of local instability of steel plates was considered by establishing a stress–strain hysteresis model for the nonlinear springs [Dang et al. 2017]. This method of concentrating all of the nonlinear deformation of pier at the bottom cannot directly reflect the damage range of structures, and this model also lacks a parameter identification method for nonlinear springs.

Based on the research status, this paper selected single-column rectangular-section steel bridge pier as its research object and extracted the average stress–strain relationship over the effective damaged zone obtained by the shell-element FE method. On the basis of the two-surface constitutive model of material, the influence of local instability was

considered by reducing elastic stiffness, setting a skeleton curve on the compressive side, and modifying the bounding surface radius, thus proposing an equivalent hysteresis model for fiber elements that can consider local instability processes of steel plates with strong universality. Through verification, the fiber model can obtain accurate calculations when the fiber element in the effective damaged zone adopts the equivalent hysteresis model proposed in this paper.

2.STRUCTURAL PARAMETERS AND MATERIAL CONSTITUTIVE MODEL OF STEEL PIERS

2.1 Steel-pier structure and design parameters

In this paper, single-column rectangular-section steel bridge pier was considered as an example. Fig. 1 shows the schematic of a single-box single-chamber rectangular-section steel-pier structure. In the Fig.1, the height of the pier, width of the section, and spacing between two diaphragms are h, B_0, and a_0, respectively. The number of subpanels separated by longitudinal stiffeners and the spacing between them are n and a_1, respectively. t and t_1 are the thicknesses of the flange plates and longitudinal stiffeners, respectively.

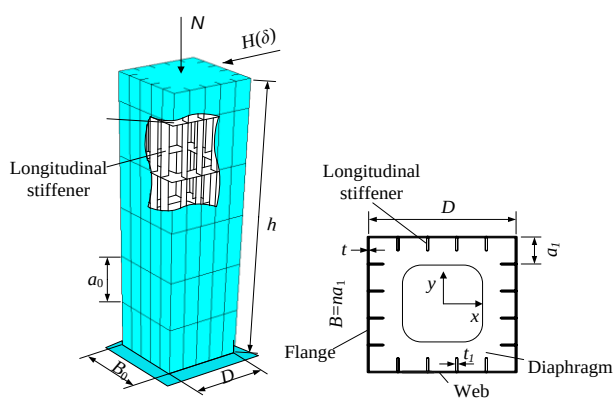

Fig. 1 Overview of steel-pier structure

The local deformation of steel plates and hysteretic behavior of rectangular-section steel piers are affected by several structural parameters such as the width-to-thickness ratio of the mother plates R_R, overall slenderness ratio λ, relative stiffness ratio of the stiffeners γ/γ^*, and spacing ratio of the diaphragms α_0. The definition of each structural parameter can be represented as follows:

$$\begin{cases} R_R = \dfrac{B_0}{t}\sqrt{\dfrac{\sigma_y}{E}\dfrac{12\left(1-\mu^2\right)}{4n^2\pi^2}} \\ \bar{\lambda} = \dfrac{2h}{\pi r}\sqrt{\dfrac{\sigma_y}{E}} \\ \gamma / \gamma^* = \dfrac{I_\lambda}{\gamma^* B t^3 / [12(1-\mu^2)]} \\ \alpha = \dfrac{a_0}{B_0} \end{cases} \tag{1}$$

where r is the radius the section gyration and γ^* is optimum relative stiffness of the longitudinal stiffener. Additionally, σ_y is material yield strength, E is material elastic modulus, and μ is Poisson's ratio.

To obtain the seismic performance of the rectangular-section steel piers with varying structural parameters, piers with different structural parameters, as shown in Tab. 1, were analyzed. In the Tab. 1, N_y represents the section's yield axial force.

Tab. 1 Structural parameters of steel piers

No.	Pier	*B*(m)	R_R	λ	α	γ/γ^*	N/N_y
1	b2	1.023	0.3924	0.3924	0.5	1	0.15
2	b3	1.344	0.5155	0.3945	0.5	3	0.15
3	b4	1.023	0.3924	0.3945	0.7	1	0.15
4	b13-10	1.023	0.3924	0.3079	0.7	3	0.1
5	b13-30	1.023	0.3924	0.3079	0.7	3	0.3

2.2 Hysteretic constitutive model of steel and its parameters

Bilinear kinematic and isotropic strengthening models, which are traditional nonlinear hysteretic constitutive models of steel, have been widely used in the seismic response analysis of steel structures because of their simplicity and good convergence. However, these models cannot consider the Bauschinger and strain hardening effects simultaneously; therefore, the calculation accuracy is low [Ge et al. 2000]. To improve calculation accuracy, this paper uses the two-surface hysteretic constitutive model [Shen et al. 1993, Shen et al. 1995]. This model was partially modified to prevent the deficiency of unreasonable hysteresis history during small strain vibrations [Wang et al. 2016].

Fig. 2 shows a stress–plastic strain hysteresis curve that is typical of the two-surface model under a uniaxial stress state. The stress is elastically loaded from origin O to yield point A; then, it enters plastic strengthening stage BC after passing through the plastic platform AB. The plastic modulus E^P of plastic zone Q1D in the opposite direction is obtained as follows:

$$E^{\mathrm{P}} = \frac{d\sigma}{d\varepsilon^{\mathrm{P}}} = E_0^{\mathrm{P}} + h\frac{\delta}{\delta_{\mathrm{in}} - \delta} \tag{2}$$

where E_0^P is the slope of the corresponding bounding surface YY′, δ is the distance from the loading point to the bounding surface, δ_{in} is the distance between the initial yield point and bounding surface during the current loading process, and h is the shape parameter, which is linear with δ:

$$h = e \cdot \delta + f \tag{3}$$

where, e and f are material constants.

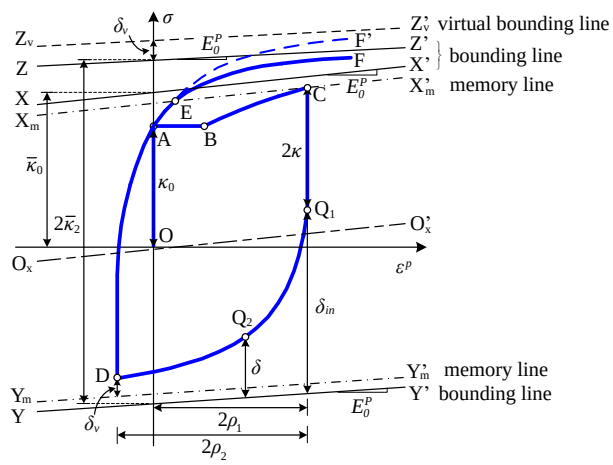

Fig. 2 Uniaxial stress (σ) –plastic strain (ε^{p}) hysteresis curve of two-surface model

To accurately predict the stress–strain hysteresis curve path, the model introduces virtual bounding and memory surfaces in addition to the bounding surface. As shown in Fig. 2, the bounding surface that corresponds to the DEF segment of the curve is ZZ′. Memory surface XmX′m is the line passing through point C with maximum historical stress and is parallel to bounding surface XX′ corresponding to point C. The distance between unloading point D and memory surface YmY′m is δ_{v}. The virtual bounding surface ZvZ′v corresponding to loading curve DEF is obtained by moving bounding surface ZZ′ along the loading direction by δ_{v}. When predicting the DE segment curve's path, the plastic modulus E^{P} is calculated as follows:

$$E^{\mathrm{P}} = E_0^{\mathrm{P}} + h\frac{\delta + \delta_{\mathrm{v}}}{\delta_{\mathrm{in}} - \delta}. \tag{4}$$

When the loading point reaches the memory surface (point E in Fig. 2), E^{P} is calculated using Equation (1) and the curve trend is DEF. This implies that the curve cannot cross the actual bounding surface ZZ′.

The model considers that the elastic range and bounding surface radii change with the equivalent cumulative plastic strain $\bar{\varepsilon}^{\mathrm{p}}$ during the loading process, which can be calculated using Equations (5) and (6), respectively:

$$\kappa = \kappa_0 \left[\alpha - a \cdot \mathrm{e}^{-100 \cdot b \cdot \bar{\varepsilon}^{\mathrm{p}}} - \left(\alpha - a - 1 \right) \cdot \mathrm{e}^{-100 \cdot c \cdot \bar{\varepsilon}^{\mathrm{p}}} \right] \tag{5}$$

$$\bar{\kappa} = \bar{\kappa}_{\infty} + \left(\bar{\kappa}_0 - \bar{\kappa}_{\infty} \right) \mathrm{e}^{-\zeta \rho^2} \tag{6}$$

Here, α, a, b, c, and ζ are parameters; κ_0 and $\bar{\kappa}_0$ are the initial elastic range and bounding surface radii, respectively; $\bar{\kappa}_{\infty}$ is the ultimate bounding surface radius, i.e., the material's ultimate strength σ_{u}; and $\rho = 0.5\bar{\varepsilon}^{\mathrm{p}}$.

This paper focuses on Q345qC structural steel for bridge, which is widely used in China. The material parameters of the two-surface constitutive model were calibrated as shown in Tab. 2 [Wang et al. 2016].

Tab.2 Material parameters of two-surface constitutive model for Q345qC [Wang et al. 2016]

$E_{\mathrm{st}}^{\mathrm{p}}$ (GPa)	$\varepsilon_{\mathrm{st}}^{\mathrm{p}}$	M	$E_{0\mathrm{i}}^{\mathrm{p}}$ (GPa)	ω (MPa^{-1})	$\bar{\kappa}_0$ (MPa)	σ_{u} (MPa)
4.47	0.0153	−0.142	1.43	0.0161	412.2	636.4
ζ	e	f (GPa)	a	b	c	α
307.4	470.0	0.53	−0.358	21.4	1.03	0.343

Note: $E_{\mathrm{st}}^{\mathrm{p}}$ and $\varepsilon_{\mathrm{st}}^{\mathrm{p}}$ indicate the plastic modulus and plastic strain, respectively, at the beginning of the strengthening stage; $E_{0\mathrm{i}}^{\mathrm{p}}$ denotes slope of the initial bounding line; and M represents parameter related to change in yield-plateau length. Remaining parameters are as described above.

4.EQUIVALENT HYSTERESIS MODEL FOR FIBER ELEMENTS IN EFFECTIVE DAMAGED ZONE OF STEEL PIERS

4.1 FE model for elastoplastic seismic response analysis of structures

To obtain the average stress–strain relationships over this length, it is necessary to extract relevant information based on the structure's seismic damage behavior. Existing studies have shown that the shell FE method can accurately reflect local instability behavior of thin-walled steel structures after they enter the elastoplastic state [Ge et al. 2000]; therefore, the FE simulation package Abaqus 6.14 was used to perform numerical analysis on the structures shown in Tab. 1 and the required information was extracted from these calculation results.

Because the local deformation of cantilevered steel piers occurs at the structure bottom, the fiber-shell hybrid element model shown in Fig. 4 was used for analysis to balance calculation accuracy and efficiency. The shell elements were used in the range of three times the diaphragm spacing at the bottom of the pier, and the upper part of the pier was modeled using fiber elements. The four-node quadrilateral shell element with reduced integration (S4R) implemented in Abaqus 6.14 was adopted in this study. There are five

integral points along the thickness direction. The type of fiber elements is two-node linear beam element in space (B31), and the fiber division of the section is shown in Fig. 5. The multi-point constraint (MPC) function was used to establish deformation relationships between the shell and fiber elements and this paper uniformly adopted the 20-layer mesh size within diaphragm spacing.

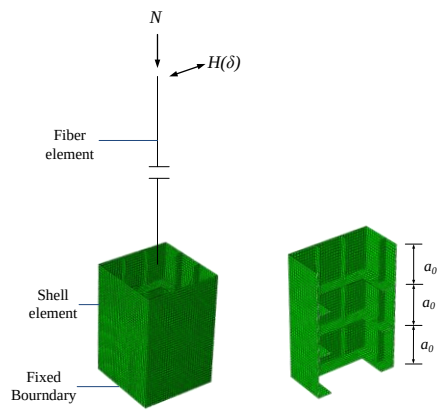

Fig. 4 FE model of steel pier

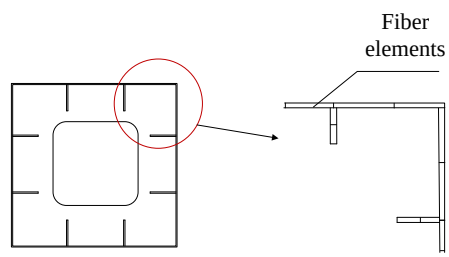

Fig. 5 Fiber division of stiffened box section

The pier is fixed at the bottom, with a constant axial force *N* and forced cyclic horizontal displacement δ applied to the top. The axial force is determined based on the axial compression ratio shown in Tab. 1. The horizontal cyclic loading form is shown in Fig. 6. The amplitude of horizontal displacement δ is applied from one time of the yield displacement δ_y, and the incremental displacement of each cycle is $0.5\delta_y$ [Tang et al. 2015].

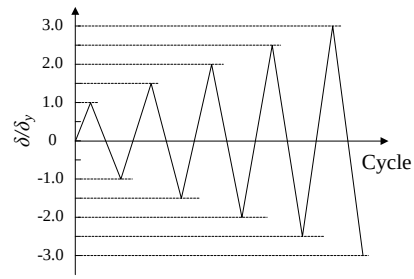

Fig. 6 Cyclic loading form

4.2 L_d and its average stress–strain relationship

Fig. 7 shows a comparison of load-displacement curves of b2 structure calculated from a hybrid element model that considers local instability of steel plates (Fig. 4) and a conventional fiber model that does not consider the local instability effect. In Fig. 7, the points (δ_m, H_m) and (δ_{80}, H_{80}) are the corresponding states when the horizontal load reaches its maximum value and falls to 80% of the maximum value in the calculation results of hybrid model, respectively. Because the fiber model does not consider local instability of steel plates, the calculation result would overestimate the structure's bearing capacity and stiffness. When structural deformation passes through the point (δ_{80}, H_{80}), the plastic deformation is too large, thus it can be considered that the structure has entered a state of destruction. Therefore, the point (δ_{80}, H_{80}) was taken as the limit state.

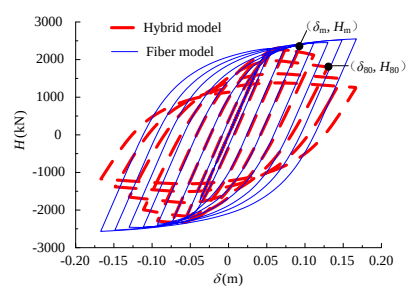

Fig. 7 Comparison of structural load-displacement history curves obtained by hybrid model and fiber model

The average strain and stress at each section point can be expressed as follows:

$$\left.\begin{aligned} \bar{\varepsilon} &= \frac{L_d - L_d^1}{L_d} \\ \bar{\sigma} &= \frac{1}{m}\sum_{i=1}^{m}\sigma_{spi} \end{aligned}\right\} \tag{7}$$

where $\bar{\varepsilon}$ is the average strain, $\bar{\sigma}$ is the average stress, and L_d is the length of the effective damaged zone, L_d^1 is the length of the effective damage zone after deformation during

cyclic loading, and σ_{spi} is the axial stress of each integral point of the shell element at the height of L_{d}. To remove the influence of the shell element's bending stress, the average stress value of *m* integration points along the thickness direction was considered as the average stress. This paper uses an *m* value of 5.

In order to calculate the seismic responses under bidirectional earthquake actions, the average stress–strain relationships extracted from all the section points over L_{d} need to be similar. Based on the results of FE analysis of the structure under cyclic loading using the different parameters in Tab. 1, it is found that the value of L_{d} is close to the length of the effective failure area of the rectangular steel piers proposed by Usami [Liu et al. 1999]. Thus, L_{d} needed in this paper can be expressed using the following formula:

$$L_{\mathrm{d}} = \min\left[0.7B, a_0\right] \tag{8}$$

To simplify the calculation, this paper uniformly used the average stress–strain relationship at point 2, which is at the corner of the section, as the objective function of the equivalent hysteresis model for the fiber element.

4.3 Equivalent hysteresis model for fiber elements considering local instability effect

It was found through calculation that after some modification, the two-surface model can also be used to fit the average stress–strain ($\bar{\sigma}-\bar{\varepsilon}$) relationship over the L_{d}. Taking piers b2 and b13-10 in Tab. 1 as examples, the average stress–strain curve of point 2 calculated using Equation (7) and the stress–strain relationship curve of the original two-surface model of Q345qC steel obtained using same strain history are shown in Fig. 8. After the local buckling phenomenon occurs in steel plates, the axial equivalent stiffness and strength decrease. Thus, some modifications are required for the original two-surface model to the fit the average stress–strain relationship. The following sections will describe this modification process.

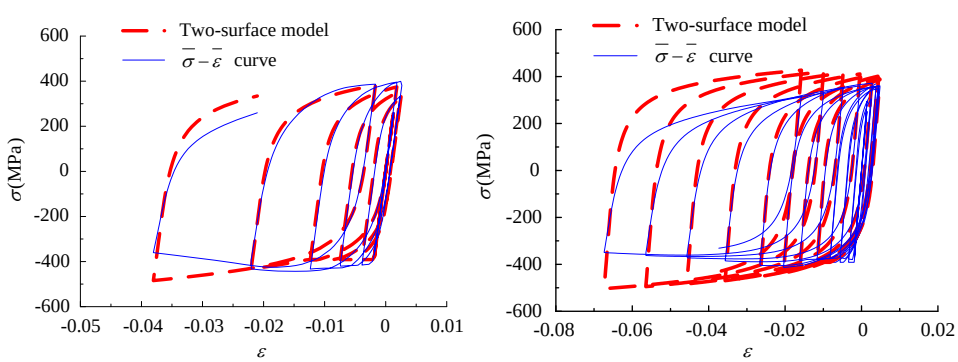

(a) Pier b2 (b) Pier b13-10

Fig. 8 Comparison of the average stress–strain relationship curve and two-surface model

Equivalent elastic modulus

Because the two-surface model is a material constitutive model established in the stress–plastic strain space, the average stress–strain curve in Fig. 8 must be transformed into an average stress–plastic strain curve. In other words, the elastic strain must be deducted from the strain.

Because of the out-of-plane geometric deformation of steel plates after local buckling, steel-plate geometric deformation is first restored when the reverse tension is applied. The slope of the average stress–strain curve elastic segments was defined as the equivalent elastic modulus, and this phenomenon is manifested by a decrease in the equivalent elastic modulus. Fig. 9 shows a graph exhibiting the relationships between the equivalent elastic modulus and current average strain of piers b2–b4, b13-10, and b13-30. When the average compressive strain is less than the average strain value corresponding to the peak displacement load value, defined as $\bar{\varepsilon}_{\mathrm{m}}$, the equivalent elastic modulus remains constant. This is basically consistent with the material's elastic modulus; otherwise, the equivalent elastic modulus is changed to the current average strain. Based on the distribution form of scatters in Fig. 12, the equivalent elastic modulus can be predicted using the following equation:

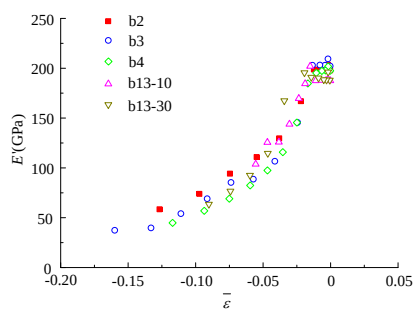

Fig. 9 Relationship between elastic modulus and current average strain

$$E' = \begin{cases} E, & \bar{\varepsilon} \geq \bar{\varepsilon}_m \\ E \cdot k \cdot e^{m \cdot \bar{\varepsilon}}, & \bar{\varepsilon} < \bar{\varepsilon}_m \end{cases} \tag{9}$$

where *E'* is the equivalent elastic modulus, *k* and m are parameters obtained by curve fitting (see "Parameter identification method for equivalent hysteresis model" for details), $\bar{\varepsilon}$ is the current average strain, and *E* is the elastic modulus of steel.

After obtaining the equivalent elastic modulus, the average plastic strain can be calculated as follows:

$$\bar{\varepsilon}^{\mathrm{p}} = \varepsilon - \frac{\bar{\sigma}}{E'} \tag{10}$$

Thus, the average stress–plastic strain curves of piers b2 and b13-10 were obtained and are shown in Fig. 10.

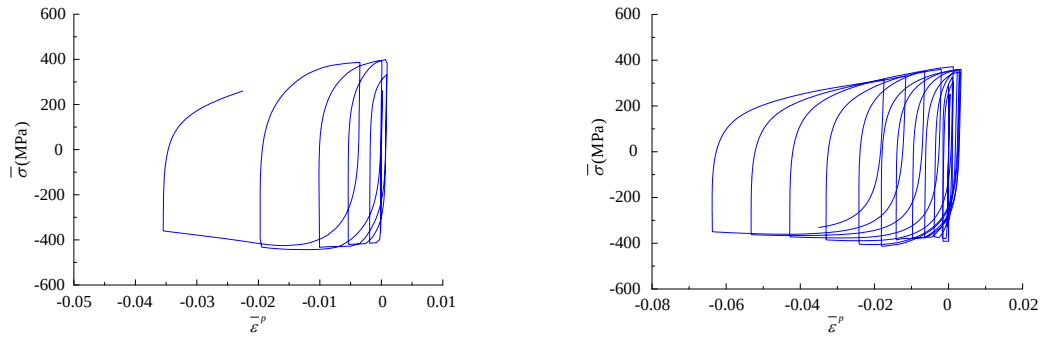

(a) Pier b2 (b) Pier b13-10

Fig. 10 Average stress–plastic strain curve

Skeleton curve in the compressive path

As shown in Fig. 10, when local buckling occurs in steel plates, structural stiffness and bearing capacity begin to decrease and the average stress–plastic strain curve in the compression area over L_d shows negative stiffness. To describe this stress–plastic strain history, this paper introduces the stress–plastic strain path ABCDE in the compression path based on the original two-surface model as shown in Fig. 11. In Fig. 11, AB represents the elastic segment, which is unchanged, and BC represents the plastic segment. The plastic modulus E^P is still calculated using Equation (2) or Equation (4). CD represents the segment in the skeleton curve and DE represents the reverse loading segment. ABD′E′ is the stress–plastic strain path calculated using the original two-surface model under the same plastic strain history and YY′ is the compressive path's bounding surface. Because the bounding surface radius of the equivalent hysteresis model considering local instability has been reduced, the bounding surface is changed to Y1Y2. Detailed rules for bounding surface radius reduction are discussed further in "Modification of the radius of bounding surface and elastic range."

In Fig. 11, the initial value of the skeleton curve M1M2N1N2 is the initial radius elastic range, σ_y. When the plastic compressive strain is greater than the peak average plastic strain $\bar{\varepsilon}_m^p$, the skeleton curve decreases as the plastic compressive strain increases with slope *AE*. It remains unchanged after reaching 0.25 times σ_y. Equation (6) shows that when the strain is equal to $\bar{\varepsilon}_m$, the equivalent elastic modulus does not need to be reduced; therefore, the peak average plastic strain $\bar{\varepsilon}_m^p$ can be calculated using the following formula:

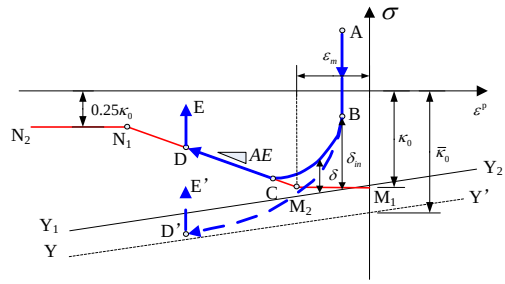

Fig. 11 Skeleton curve and stress–plastic histories before and after compressive path modification

$$\bar{\varepsilon}_{\mathrm{m}}^{\mathrm{p}} = \bar{\varepsilon}_{\mathrm{m}} - \frac{\sigma_{\mathrm{y}}}{E} \tag{11}$$

Modification of the radius of bounding surface and elastic range

As shown in Fig. 10, after local instability occurs, the bounding surface shrinks toward the center and the elastic range radius decreases. Therefore, the bounding surface and elastic range in the equivalent hysteresis model must be modified. First, the modified radius $\bar{\kappa}_0^1$ of the initial bounding surface is expressed as follows:

$$\bar{\kappa}_0^1 = B \cdot \bar{\kappa}_0 \tag{12}$$

where *B* is a model parameter.

The bounding surface radius can be calculated by substituting $\bar{\kappa}_0^1$ for $\bar{\kappa}_0$ in Equation (6). The bounding surface shrinks because of local instability; therefore, the bounding surface radius decreases by the following formula:

$$\bar{\kappa}_1 = \bar{\kappa} - \left(\bar{\varepsilon}_{\mathrm{m}}^{\mathrm{p}} - \bar{\varepsilon}_1^{\mathrm{p}}\right) C \cdot E \tag{13}$$

where C is a model parameter, $\bar{\kappa}_0$ is the average plastic strain from the previous compression-to-tension point in the history, $\bar{\kappa}_1$ is the radius of bounding surface after reduction.

After determining the radius of the reduced bounding surface, the radius of the reduced elastic range can be calculated directly as follows:

$$\kappa_1 = \kappa - \frac{\left(E_0^{\mathrm{p}} + A \cdot E\right)\left(\bar{\varepsilon}_{\mathrm{m}}^{\mathrm{p}} - \bar{\varepsilon}_1^{\mathrm{p}}\right) + \left(\bar{\varepsilon}_{\mathrm{m}}^{\mathrm{p}} - \bar{\varepsilon}_1^{\mathrm{p}}\right) C \cdot E}{2} \tag{14}$$

In Equation (14), κ is the radius of elastic range obtained using Equation (5) and κ_1 is the elastic range radius after reduction. The meanings of the remaining parameters are consistent with previous equations.

Fig. 12 is a graph showing the stress–plastic strain relationship of the equivalent hysteresis model obtained using the modification methods for piers b2 and b13-10. Further, the bounding surfaces before and after the modification are given. Compared with the average stress–plastic strain curves obtained using the fine FE calculation, after the modification for the original two-surface model described in the sections titled “Equivalent elastic modulus,” “Skeleton curve in the compressive path,” and “Modification of the radius of bounding surface and elastic range,” the equivalent hysteresis curves are basically the same as the corresponding average stress–plastic strain curve extracted from the fine FE calculation result.

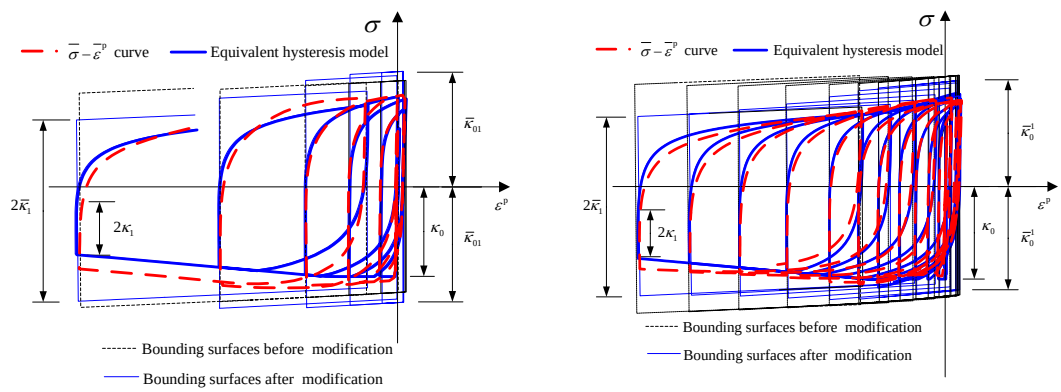

(a) Pier b2 (b) Pier b13-10

Fig. 12 Comparison of the stress–plastic strain curve of the equivalent hysteresis model and average stress–strain curve

4.4 Parameter identification method for equivalent hysteresis model

In the proposed equivalent hysteresis model, state variables such as virtual bounding surface, memory surface, and yield platform are determined using the same method as original two-surface model, and the parameter $\bar{\varepsilon}_{\mathrm{m}}^{\mathrm{p}}$ is calculated using Equation (11). The methods for determining the other five model parameters (*A*, *k*, *m*, *B*, and *C*) in the model are discussed below.

Parameter A

Parameter *A* is obtained from the average plastic stress–strain relationship. Considering pier b13-10 as an example, Fig. 13 shows the parameter *A* determination process. Point M2 is the turning point of the skeleton curve, which is the same as point M2 in Fig. 11, and has co-ordinates $\left(\bar{\varepsilon}_{\mathrm{m}}^{\mathrm{p}}, -\sigma_{\mathrm{y}}\right)$. *AE* is the slope of the line connecting the

co-ordinates of point M2 and compression-to-tension point M3 $\left(\bar{\varepsilon}_{\mathrm{f}}^{\mathrm{p}}, -\sigma_{\mathrm{f}}\right)$ with the largest compressive strain. Thus, parameter *A* can be determined as follows:

$$A = \frac{\sigma_{\mathrm{y}} - \sigma_{\mathrm{f}}}{E\left(\bar{\varepsilon}_{\mathrm{f}}^{\mathrm{p}} - \bar{\varepsilon}_{\mathrm{m}}^{\mathrm{p}}\right)} \tag{15}$$

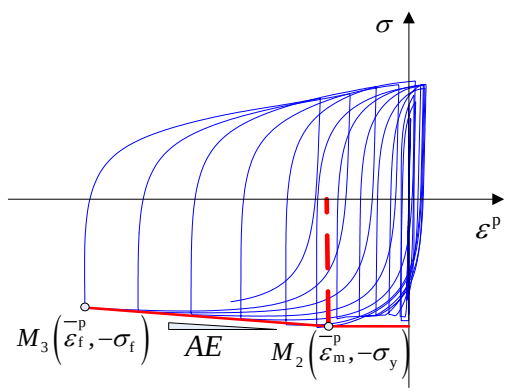

Fig. 13 Determination of parameter A

Parameters k and m

Considering pier b2 as an example, the data points of the equivalent elastic modulus were extracted from the average stress–strain curve. Fig. 14 shows these data points and a fitted expression of the equivalent elastic modulus based on Equation (9). Parameter *k* of pier b2, corresponding to Q345qC steel, is 217.8 and *m* is 11.49. When different materials and other structures are involved, the same method can be used to obtain the fitting results for parameters *k* and *m*.

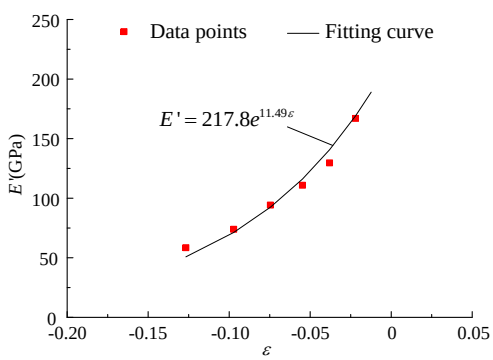

Fig. 14 Determination of parameters k and m

Parameters B and C

After obtaining parameters $\bar{\varepsilon}_{\mathrm{m}}^{\mathrm{p}}$, *k*, *m*, and *A*, parameters *B* and *C* can be calculated by optimization using Equation (16) as the objective function:

$$\sum_{n=1}^{n_0}\left[\bar{\sigma}\left(\bar{\varepsilon}_k\right)-\bar{\sigma}^*\left(\bar{\varepsilon}_k\right)\right]^2 \rightarrow \min \tag{16}$$

where n_0 is the number of discrete points in the average stress–plastic strain curve and *n* is the order of each discrete point. $\bar{\sigma}$ and $\bar{\sigma}^*$ are the average stress extracted from the hybrid element model and stress calculated using the equivalent hysteresis model, respectively. In this paper, parameters *B* and *C* were fitted using an average stress–strain curve before the bearing capacity dropped to 80% of the maximum. An adaptive genetic algorithm was employed for the optimization calculations of Equation (16).

Tab. 3 lists the six equivalent hysteresis model parameters for each pier in Tab. 1.

Tab.3 Parameter identification results of equivalent hysteresis model

Pier	$\bar{\varepsilon}_{\mathrm{m}}^{\mathrm{p}}$	*a*	*k*	*m*	*c*	*d*
b2	0.008	0.0169	1.065	11.49	1.092	0.0369
b3	0.008	0.0113	1.067	13.5	1.097	0.0386
b4	0.0119	0.0177	1.154	16.03	1.044	0.0422
b13-10	0.015	0.00739	1.230	16.47	1.037	0.02067
b13-30	0.019	0.0135	1.710	21.36	0.929	0.0364

5.VALIDITY VERIFICATION OF THE EQUIVALENT HYSTERESIS MODEL

To verify the calculation accuracy of the fiber model proposed in this paper, five piers in Tab. 1 were used as examples to compare structural seismic response calculation results obtained using the fine hybrid and fiber models using the equivalent hysteresis model. Fig. 15 shows the calculation models for these two algorithms. Fig. 15(a) represents the calculation model with fiber-shell hybrid elements, in which fine shell elements were modeled in the bottom where local instability may occur and fiber elements were used in other parts. Fig. 15(b) shows the fiber calculation model proposed in this paper, in which a fiber element was established in the effective damaged zone. The equivalent hysteresis model established in this paper was used in this fiber element and model parameters were determined in Tab. 3. The material's two-surface constitutive model was used in the remainder of the structure. Axial force in the static model was converted to the pier mass m_0, and the quasi-static load still adopted the loading form shown in Fig. 6. Ground motions were input at the bottom of the pier in one and two directions along the principal axis of the cross section, respectively. The ground motion input used was the acceleration wave from the Niigata earthquake in Japan recorded in Ojiya (2004). The EW and NS acceleration waves and response spectrum are shown in Fig. 16; *A* represents acceleration and *SA* represents the acceleration response spectrum. In the horizontal unidirectional calculation, only the EW wave was input in the X direction. In the horizontal bidirectional seismic response calculation, the EW and NS waves are input in the X and Y directions,

respectively. The appropriate peak ground accelerations (PGA) were adjusted when different structures were analyzed.

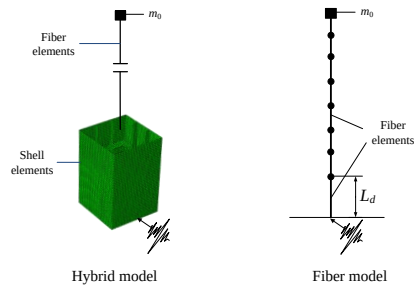

Fig. 15 Calculation model for seismic response of steel pier

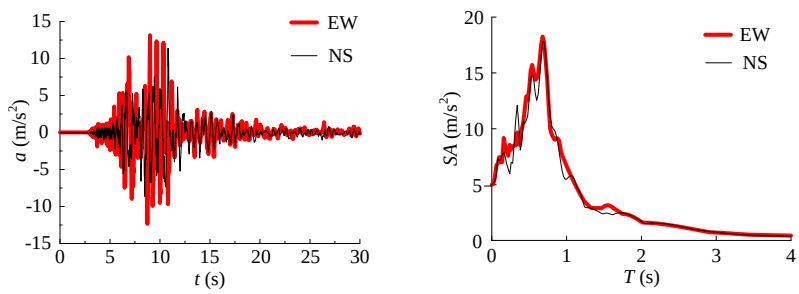

Fig. 16 Earthquake acceleration curve and response spectrum

Fig.s 17–21 show comparisons of the five sets of components, where δ_X and δ_Y are the displacement responses in the X and Y directions, respectively. The calculation results of the graphs show that regardless of whether under a static, horizontal unidirectional, or bidirectional load, the calculation results of fiber models can be quite similar to that of the fine hybrid model if the fiber elements in L_d adopt the proposed equivalent hysteresis model. Computational accuracy is significantly improved compared with the traditional fiber model (see Fig. 7); however, calculation efficiency is basically unchanged. Thus, it is verified that the proposed equivalent hysteresis model for fiber elements and the corresponding calculation method have good accuracy and availability.

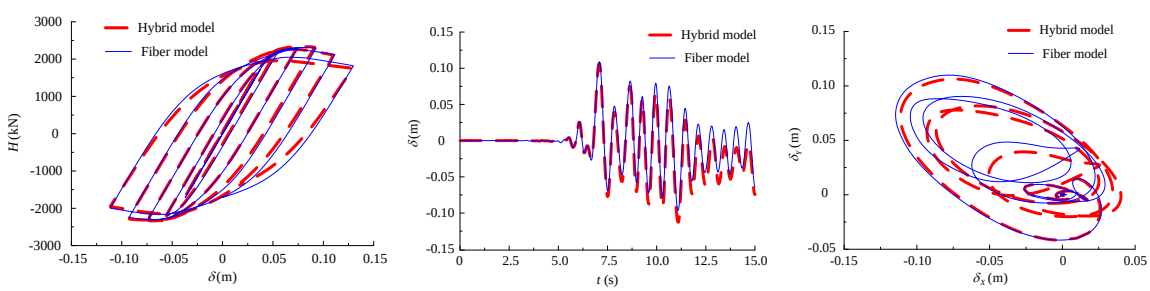

(a) Static (b) Uni-direction dynamic, PGA = 0.5 g (c) Bi-direction dynamic, PGA = 0.5g
Fig. 17 Calculation results comparison for pier b2

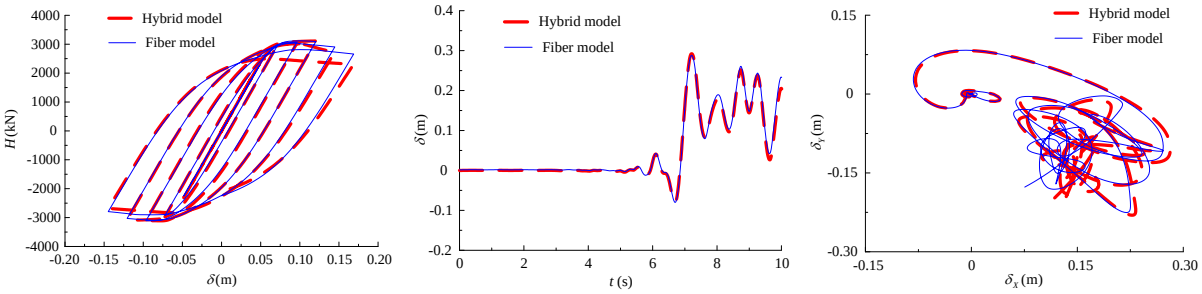

(a) Static (b) Uni-direction dynamic, PGA = 0.8g (c) Bi-direction dynamic, PGA = 0.8g
Fig. 18 Calculation results comparison for pier b3

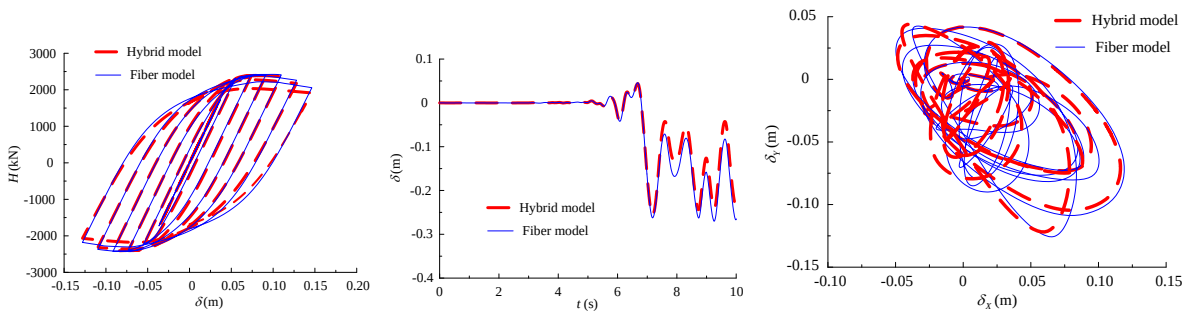

(a) Static (b) Uni-direction dynamic, PGA = 0.8g (c) Bi-direction dynamic, PGA = 0.5g
Fig. 19 Calculation results comparison for pier b4

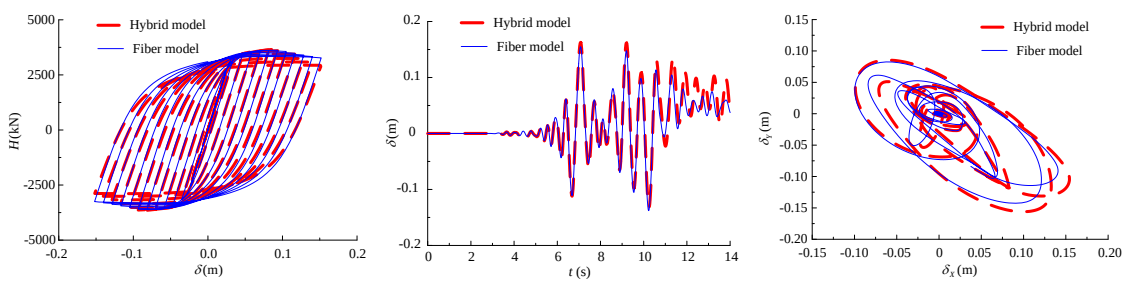

(a) Static(b)Uni-direction dynamic, PGA = 1.3g(c) Bi-direction dynamic, PGA = 1.3g
Fig. 20 Calculation results comparison for pier b13-10

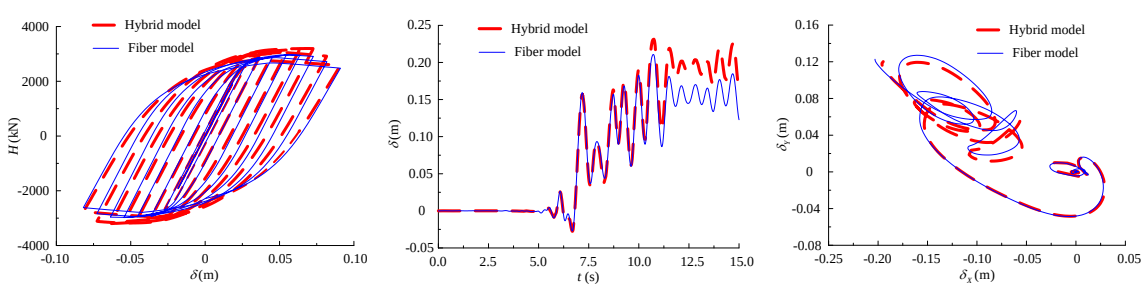

(a) Static (b) Uni-direction dynamic, PGA = 0.5g (c) Bi-direction dynamic, PGA = 0.5g
Fig. 21 Calculation results comparison for pier b13-30

6. CONCLUSION

In this paper, an equivalent hysteresis model for fiber elements in the seismic effective damaged zone was established using single-column rectangular-section steel piers as study objects. A calculation method based on fiber model for steel piers that can consider local instability effects of steel plates is proposed. This research reached the following conclusions:

(1) By determining a reasonable length of effective damaged zone, the average stress–strain relation of each section point is basically independent of the section points position, thus meeting the horizontal bidirectional seismic response calculation requirements of piers.

(2) By introducing the equivalent elastic modulus and skeleton curve and reducing the bounding surface radius, an equivalent stress–strain hysteresis model was established based on the two-surface constitutive model. Additionally, a method for identifying the model parameters was proposed.

(3) The model were verified through comparison with the calculation results of the fiber-shell hybrid model. This paper provides a method for calculating the elastoplastic seismic response with high calculation accuracy, with good availability for the seismic design of steel piers under horizontal bidirectional earthquake actions.

References

Kawashima K, Unjoh S, The damage of highway bridges in the 1995 Hyogo-Ken Nanbu earthquake and its impact on Japanese seismic design. *Journal of Earthquake Engineering*, 1997, **1**(3): 505-541.

Usami T. *Guidelines for seismic and damage control design of steel arch bridges*. Tokyo: Gihodo Shuppan Co. Ltd., 2007.

Ge HB, Gao SB, Usami T, Matsumura T. Numerical study on cyclic elasto-plastic behavior of steel bridge piers of pipe-sections without stiffeners. Proc JSCE 1997;**577**:181–90. [in Japanese].

Ge HB, Gao SB, Usami T. Stiffened steel box columns. Part 1: Cyclic behaviour. *Earthquake Engineering and Structural Dynamics*, 2000;**29**(11):1691–1706.

Usami T, Gao SB, Ge HB. Stiffened steel box columns. Part 2: Ductility evaluation. *Earthquake Engineering Structural Dynamics*, 2000;**29**(11):1707–1722.

Usami T, Gao SB, Ge HB. Elastoplastic analysis of steel members and frames subjected to cyclic loading. *Engineering Structures*, 2000;**22**(2):135–145.

Watanabe E, Sugiura K, Oyawa WO. Effects of multi-directional displacement paths on the cyclic behaviour of rectangular hollow steel columns. *Journal of Structural Engineering and Earthquake Engineering*, 2000;**17**(1):79-95.

Goto Y, Jiang KS, Obata M. Stability and ductility of thin-walled circular steel columns under cyclic bidirectional loading. ASCE *Journal of Structural Engineering*, 2006;**132**(10):1621–1631.

Goto Y, Muraki K, Obata M. Ultimate state of thin-walled circular steel columns under bidirectional seismic accelerations. ASCE *Journal of Structural Engineering*, 2009; **135**(12): 1481-1490.

Goto Y, Jiang KS, Obata M. Hysteretic behavior of thin-walled stiffened rectangular steel columns under cyclic bi-directional loading. Proc JSCE A 2007;**63**(1):122–141.[in Japanese].

Goto Y, Koyama R, Fujii Y, et al. Ultimate state of thin-walled stiffened rectangular steel columns under bi-directional seismic excitations. JSCE Ser. A1, 2009, **65**(1): 61–80.

Kulkarni NG, Kasai A, Tsuboi H. Displacement based seismic verification method for thin-walled circular steel columns subjected to bi-directional cyclic loading. *Engineering Structures*,2009;**31**(11):2779–2786.

Kulkarni N, Kasai A. Seismic verification method for steel bridge piers with pipe section under two directional earthquake components. JSCE Ser. A1 2012;**68**(3):597–609.

Wang M, Shi YJ, Wang YQ. Equivalent constitutive model of steel with cumulative degradation and damage. *Journal of Constructional Steel Research*, 2012;**79**:101–114.

Noriko KODAMA and Teruhiko YODA. Dynamic response analysis of box section steel frames considering local buckling, Proc JSCE 2003;No. **731/I-63,** 169-184.

Dang J, Yuan HH, Igarashi A, et al. Multiple-spring model for square-section steel bridge columns under bidirectional seismic load[J]. ASCE *Journal of Structural Engineering*, 2017, **143**(5):04017005-1–15.

Shen C, Mizuno E, Usami T, A generalized two-surface model for structural steels under cyclic loading, JSCE *Journal of Structural Mechanics and Earthquake Engineering*,1993;**471** (I-2):23–33.

Shen C,Mamaghani I,Mizuno E, et al., Cyclic behavior of structural steel, II: theory, ASCE *Journal of Engineering Mechanics*,. 1995; **121** (11), 1165–1172.

Wang T, Xie X, Shen C, Tang ZZ, Effect of hysteretic models on elasto-plastic seismic performance evaluation of a steel arch bridge, *Earthquake and Structures* 2016 ;**10** (5), 1089–1109

Tang ZZ, Xie X, Wang T, et al. Study on FE models in elasto-plastic seismic performance evaluation of steel arch bridge. *Journal of Constructional Steel Research*, 2015; **113**: 209–220.